

Generation and Analysis of Wire Rope Digital Radiographic Images

S Chakhlov¹, P Anpilgov², A Batranin³, S Osipov⁴, Sh Zhumabekova⁵ and I Yadrenkin⁶

¹Head of Laboratory, National Research Tomsk Polytechnic University, Tomsk, Russia

²Expert, LLC “Tepromes”, Tomsk, Russia

³Junior Researcher, National Research Tomsk Polytechnic University, Tomsk, Russia

⁴Leading Researcher, National Research Tomsk Polytechnic University, Tomsk, Russia

⁵Student, National Research Tomsk Polytechnic University, Tomsk, Russia

⁶Assistant, Tomsk State University of Architecture and Building, Tomsk, Russia

E-mail: chakhlov@tpu.ru

Abstract. The paper is dealt with different structures of the digital radiographic system intended for wire rope radiography. The scanning geometry of the wire rope is presented and the main stages of its digital radiographic image generation are identified herein. Correction algorithms are suggested for X-ray beam hardening. A complex internal structure of the wire rope is illustrated by its 25 mm diameter image obtained from X-ray computed tomography. The paper considers the approach to the analysis of digital radiographic image algorithms based on the closeness of certain parameters (invariants) of all unit cross-sections of the reference wire rope or its sections with the length equaling to the lay. The main invariants of wire rope radiographic images are identified and compared with its typical defects.

1. Introduction

For the last few decades, non-destructive testing techniques have been rapidly developed, including those applied for wire ropes. NDT techniques used for detecting manufacturing and operational defects of wire ropes include various optical, magnetic, ultrasonic, electrical, and other methods [1–3]. Wire ropes with large diameter are the most complicated test objects for NDT testing. Such objects can be tested by classical radiography which has a number of disadvantages, namely: the use of argentine-containing radiographic films that results in a high cost of testing and the extremely low performance due to the multi-stage and long-term formation of shadow images. Since the 80s of the past century, the different implementations of digital radiography have been rapidly developed [4–7] that are characterized by high performance, sensitivity, and the possibility of applying various algorithms of image processing. Radiometric detectors provide the generation of radiographic images having the geometrical resolution close to classical radiography. And a wider classification of high-performance X-ray sources stipulate for the use of radiography in NDT of wire ropes possessing large diameters [8–11].



2. Structures of the digital radiographic system

The digital radiographic image of a wire rope is generated by its scanning with a narrow X-ray beam produced by a slit collimator. Two scanning variants are possible. The first implies the wire rope movement relative to an X-ray generator-detector static system. In the second variant, this system moves relative to a wire rope in a static condition.

Wire rope scanning can be carried out by two ways: discrete and continuous. In discrete scanning, the mutual movement of the test object and the X-ray generator-detector static system is performed by fixed steps Δl . In continuous scanning, the line is formed during the time interval Δt . The parameters of discrete and continuous scanning relate to each other as $\Delta l = V\Delta t$, where V is the velocity of the wire rope movement relative to the X-ray generator. Radiographic image formation using pulsed X-ray sources can be performed solely by the integration method of radiation recording, while in a continuous X-ray source, both the integration and counting methods are possible. The counting method includes different implementations, namely: counting method proper; time; spectral.

3. Layout geometry of scanning a wire rope

Figure 1 presents the cross-sectional view of the digital radiographic system and continuous scanning with a narrow X-ray beam similar to that one described in the work of Osipov et al. [10]. The test object, namely the wire rope, can be represented by a steel cylinder with radius R . For convenience, let us assume that all line-scan detectors are oriented towards the X-ray source.

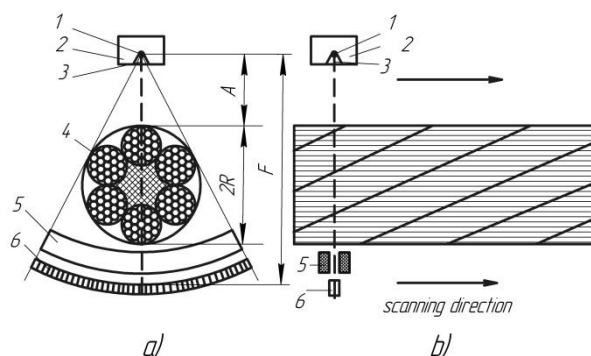


Figure 1. Cross-sectional view of digital radiographic system:

(a) normal to the scanning direction; (b) in the scanning direction.

1 – X-ray source; 2 – biological protection unit; 3 – embedded slit collimator;

4 – test object; 5 – slit collimator; 6 – detector array.

Single radiometric detectors in the array have the cross-sectional dimension of $a \times a$ and are located at distance F from the X-ray source. The additional properties of the digital radiographic system are the minimum distance A from the X-ray source to the test object and the arc length l which touches frontal surfaces of detectors. The original digital image I is $N \times M$ size matrix, where N is the number of pixels in length and $N = l/\Delta l = l/(V\Delta t)$; M is the number of detectors in the array. Let us assume that $M \ll N$. In case the detectors adhere to each other, the geometrical parameter l can be obtained from the formula

$$l \approx Ma \quad (1)$$

In radiographic systems based on pulsed X-ray sources, M is selected with a glance to the necessity for the use of end detectors in the capacity of reference channels intended for calibration

$$M > \text{int}(2F \arcsin(R/(R+A))/a + 0.5) + 2k + 2, \quad (2)$$

where R is the radius of the rope; k is the number of end detectors in the array that excludes the hypothetical shadowing of line-scan detectors by the test object.

4. Generation of digital radiographic images

Let us assume that detector m , $m=1\dots M$ has two parameters, namely k_m and σ_m , i.e. the amplification coefficient and the inherent noise level, respectively. The wire rope is scanned by a narrow radiation beam produced by a slit collimator with the maximum energy E_{max} . The X-ray source is not isotropic. Therefore, it is necessary to reduce the influence of individual detector properties on the quality of final images. This can be achieved by both black and white calibration. Black calibration measurements are carried out at switched off X-ray source I_b , whilst white calibration measurements are carried out at switched on X-ray source I_w and without a test object. The original image I is formed with the test object. The number of lines N_b and N_w in images I_b and I_w is significantly lower than N .

By means of the analog-to-digital coder, a set of analog signals (images) I_b, I_w, I transforms to a set of digital signals (images) J_b, J_w, J . This process is described by equations

$$\begin{aligned} J_{nm} &= [I_{nm}/\Delta I], \quad n=1 \div N, \quad m=1 \div M; \quad J_{bnm} = [I_{bnm}/\Delta I], \\ & \quad n=1 \div N_b; \quad J_{wnm} = [I_{wnm}/\Delta I], \quad n=1 \div N_w \end{aligned} \quad (3)$$

where $[x]$ is the integral part of x value; ΔI is the quantization interval. The quantization interval ΔI is connected to the capacity k of the analog-to-digital coder $\Delta I = I_{lim}/2^k$, where I_{lim} is the maximum possible level of signals received from radiometric detectors. In case of pulsed X-ray sources, images J_w, J are additionally normalized by the signal from the reference channel.

At the next stage, a digital radiographic image Y is composed from J_b, J_w, J images:

$$Y_{nm} = \ln(J_{0m} - \sigma_m) - \ln(J_{nm} - \sigma_m), \quad \sigma_m = \sum_{n=1}^{N_b} J_{bnm} / N_b, \quad J_{0m} = \sum_{n=1}^{N_w} J_{wnm} / N_w. \quad (4)$$

The final digital image Y can be analyzed by an operator or a specialized algorithm oriented to the detection, identification, and estimation of the defect impact degree. In the first case, the image Y is transformed to a digital gray-scale picture Y_{GS}

$$Y_{GS\ nm} = M_{hl} (Y_{nm} - S_b) / (S_w - S_b), \quad (5)$$

where S_b, S_w are respectively black and white levels in Y image; M_{hl} is the number of halftones or gray gradations. The approach, when $S_b = \min_{n,m} Y_{nm}$, $S_w = \max_{n,m} Y_{nm}$ at $m=1\dots M$; $n=1\dots N$, seems to be more expedient.

The halftone image Y_{GS} is analyzed to detect defects and estimate their validity. The image obtained by the X-ray computed tomography is presented in Figure 2 which illustrates the arrangement of strands in wire rope having the diameter of 25 mm.

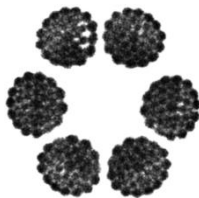


Figure 2. CT-scan image of the wire rope.

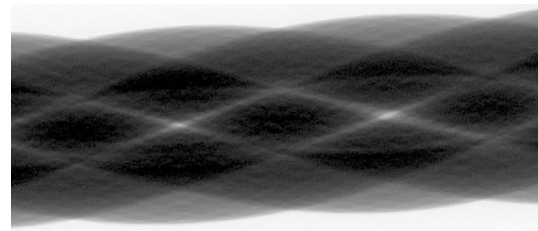


Figure 3. A typical digital radiographic image of wire rope.

The image analysis of wire rope CT-scans is difficult for an operator due to a heterogeneous distribution of intensity in the image. These difficulties can be eliminated by the use of specialized algorithms calculated for processing the radiographic images as described, for example, in the work of Osipov *et al.* [8].

A digital radiographic image of the wire rope with the internal structure shown in Figure 2 is presented in Figure 3. The experiment was carried out on the tomograph with X-ray tube 0.4 mm focal spot, 450 kV voltage; and the PerkinElmer X-ray detector having 200 μm pitch. The best results were obtained at 200 keV radiation energy with the use of filter consisting of a 2 mm thickness sheet of copper and 2.2 projection magnification.

5. X-ray beam hardening correction algorithm

The traditional equation for the radiometric signal I and the thickness ρH (g/cm^2) of the attenuation material is as follows [12]:

$$I/I_0 = e^{-m_{ef}(E_{max}, \rho H)\rho H}, \quad (6)$$

where $m_{ef}(E_{max}, \rho H)$ is the mass attenuation coefficient of photons having energy E_{max} ; I_0 is the radiometric signal without a test object.

It is obvious that X-ray beam hardening correction algorithm is reduced to the estimation of ρH parameter. The following main methods are used to calculate the correction algorithm: graphic, inverse functions, analytical approximations, and dual energy X-ray imaging.

$$m_{ef}(E_{max}, \rho H)\rho H = -\ln(I/I_0) = Y = F(\rho H). \quad (7)$$

The graphic method includes the construction of the function $F(\rho H)$ graph by the results of experimental research or mathematical simulation. The function $F(\rho H)$ graph is constructed for the fixed scanning geometry and pre-set E_{max} value. ρH is X -axis and F is Y -axis. The intersection point of the line is $Y=Y_1$, where Y_1 is the measured signal, and the curve $F(\rho H)$ is just the target value of the thickness ρH that corresponds to Y_1 signal.

The method of inverse functions estimate the thickness ρH from

$$\rho H = F^{-1}(Y), \quad (8)$$

where F^{-1} is the inverse function. Let parameter ρH takes values of $\rho H_1, \rho H_2, \dots, \rho H_n$ which correspond to signal values of Y_1, Y_2, \dots, Y_n . In case the measuring signal takes Y value, the value of ρH_i can serve as a crude estimate of ρH target value for which the deviation of $|Y_k - Y|$ at $k=1..n$ is minimum. The more accurate ρH measurement can be provided by the linear interpolation

$$\rho H \approx \rho H_i + (Y - Y_i)(\rho H_{i+1} - \rho H_i)/(Y_{i+1} - Y_i). \quad (9)$$

In case the value n is large and calibration thicknesses $\rho H_1, \rho H_2, \dots, \rho H_n$ are close to each other, ρH value obtained from equation 9 can be rather exact. Also, it will be more exact if measured by spline interpolation as described by Chen *et al.* [13], the function F^{-1} being interpolated. Spline interpolation factors $a_i, b_i, c_i, d_i, i=1..n$ are at stages of calibration measurements.

The analytical approach is based on the description of $Y(\rho H)$ function:

$$Y(\rho H) = \left(1 + A/(1 + B\rho H + C(\rho H)^2)\right)D\rho H, \quad (10)$$

where A, B, C, D are approximation coefficients depending on E_{max} , effective atomic number of the attenuation material Z , the detector sensitive volume, etc. equation 10 is the approximation refinement as described in works [12, 14]. Coefficients A, B, C, D are ascertained at a stage of calibration. In the course of the formation and transformation of the radiographic image for each of its point, equation 10 can be solved with its left side measured relative to the known ρH value. In order to rapidly solve solutions similar to (10), the abovementioned method of inverse functions can be used.

In terms of wire rope applications, the dual-energy X-ray imaging is considered in detail in works of Dai *et al.* [9] and Osipov *et al.* [10]. A method of correction of the factor under analysis is chosen by the rope diameter and the requirements for the detection and identification of its defects as well as their validity. The dual-energy X-ray imaging is the most universal method in this case.

Image Y^* formed at the algorithm output can be obtained from

$$Y^* = \{ \rho H_{nm}^*; m = 1 \dots M; n = 1 \dots N \}. \quad (11)$$

Further, it is image Y^* that is subjected to processing with a view to detect defects of the channels, and carry out their identification, and rationale for validity.

6. The analysis of digital radiographic images of wire ropes

Osipov *et al* [8, 10] suggested the approach to the analysis of digital radiographic image algorithms based on the closeness of certain parameters of all unit cross-sections of the reference wire rope or its sections with the length equaling to the lay. Let these parameters be invariants of the wire rope, and in relation to radiographic images – invariants of radiographic images of wire ropes. Let us give several preliminary apparent notes connected to certain invariants of radiographic images based on Figure 3.

Note 1. There is a symmetric axis of the wire rope shadow image. The presence a symmetric axis generates the existence of a range of invariants of digital radiographic images of wire ropes. Let us introduce the coordinate system OXY in the wire rope image. Axis OX is the symmetric axis of the shadow rope image. Let us introduce $f_1(x)$ and $f_2(x)$ functions that restrict the wire rope image at the top and at the bottom. Thus, Note 2 can be stated to introduce $f_1(x)$ and $f_2(x)$ functions.

Note 2. Functions $f_1(x)$ and $f_2(x)$ are periodical and connected by $f_1(x) = -f_2(x)$ relation.

Invariants defined by $f_1(x)$ and $f_2(x)$ functions include: maximum transverse size D_{max} of the rope shadow in image; minimum transverse size D_{min} of the rope shadow in image; distance L between locations of the adjacent maxima and minima of these functions.

Strand boundaries are rather clearly seen in Figure 3. The additional invariants are connected with this fact and the significant difference between the maximum brightness of image fragments Y_f . For example, the distance L_w between the white spot centers located on the axis of the shadow image can be chosen as invariant.

One more note is connected with the stability of a certain mass property of the wire rope. It is obvious that the rope sections of the similar length have the similar weight. Let us reformulate this note in terms of the analysis of the final radiographic image of the wire rope.

Note 3. The weight W of the wire rope section limited by the X-ray radiation beam, stays practically unchanged during the formation of the unit line of the final radiographic image.

Let W be the mass of the rope cross-section. The analysis of classical radiographic images or of the dual energy images (Equation 11) allows the accurate measurement of the rope cross-section [15].

The digital radiography provides the solution of such problems as determination of different defects; measurement of defect sizes both in the scanning direction and the direction normal to it; identification of defects. In the work of Osipov *et al* [8], the approaches to the defect identification of wire ropes are considered, namely: broken wire, wear, squashing, local increase of wire rope diameter, corrosion. These approaches are based on the defect formation. Apparently, the identification of certain defect types can be directly connected with the analysis of deviations from reference values (index *nor*, see Table 1) of radiographic image invariants. The Table 1 below presents the more widespread defect types with the abovementioned invariants for wire ropes with fiber cores. Also, visual defect characters and recommendations are given for the use of additional or alternative testing techniques.

7. Conclusion

Equations (1)–(11) sequentially describe distinctive properties of generation and analysis of digital radiographic images of wire ropes allowing to use them for further research that concerns calculations of the image processing algorithm and wire rope proper identification. Results obtained will foster the improvement of NDT techniques in relation to wire rope in-process and in-service testing and the increase of their safety and durability.

Table 1. Invariants of radiographic images and main types of defects.

Main invariants	Defects	Defect visualization
Gradual change of brightness in image fragments	Broken wire	White spot on the background, $Y_F > Y_{nor}$
Maximum transverse size of the rope shadow in the image	Squashing	$D_{max} > D_{nor}$ or $D_{max} < D_{nor}$, but $W \approx W_{nor}$
Mass of the rope cross-section	Wear	$W < W_{nor}$
Maximum transverse size of the rope shadow in the image	Local increase of wire rope diameter	$D_{max} > D_{nor}$, $W \approx W_{nor}$, brightness of the central part is close to the reference, brightness difference increase in image fragments
	Internal corrosion of wire rope	$D_{max} > D_{nor}$, $W \approx W_{nor}$, different brightness in image fragments. Dual energy X-ray imaging is recommended
	Local diameter reduction due to a fiber core	$D_{max} < D_{nor}$, $W \approx W_{nor}$
Image symmetry	Foreign inclusions	$D_{max} > D_{nor}$ and $W > W_{nor}$
	Wire rope rupture	Asymmetric distortion or formation of darker areas in the image. Several camera angles are recommended
Brightness of image fragments	Separate strand or wire pushing out	$D_{max} > D_{nor}$. Several camera angles are recommended
Distance between centres of white spots located on the axis of the shadow image	Wire rope extension	$L_w > L_{w\,nor}$ and $L > L_{nor}$, $\Sigma W = \Sigma W_{nor}$

Acknowledgements

The authors acknowledge the financial support of the Ministry of Education and Science of the Russian Federation for carrying out this research.

References

- [1] Zhang D *et al* 2013 *J. Nondestruct. Eval.* **32** 37–43
- [2] Krešák J *et al* 2012 *Metalurgija-Zagreb* **51** 485–488
- [3] Hua-Ming L and Yi-Mei M 2013 *Rus. J. Nondestruct. Testing* **49** 602–609
- [4] Liu H P, Miao C Y and Li X G 2013 *Adv. Mat. Res.* **722** 572–575
- [5] Xian-Guo L *et al* 2012 *Int. J. of Digital Content Technology and its Applications* **6** 226–234
- [6] Ewert U *et al* 2010 *Mater. Eval.* **68** 163–168
- [7] Ewert U *et al* 2012 *Mater. Eval.* **70** 955–964
- [8] Osipov S P *et al* 2013 *Tekhnologii Tekhnosfernoi Bezopasnosti* **51**
- [9] Dai Y, Miao C and Rong F F 2009 *Int. Symp. Photoelectronic Detection and Imaging: International Society for Optics and Photonics* **7385**
- [10] Osipov S P *et al* 2012 *Tekhnologii Tekhnosfernoi Bezopasnosti* **44**
- [11] Sidulenko O A *et al* 2007 *Instruments and Systems: Monitoring, Control, and Diagnostics* **3** 62–64
- [12] Nedavnii O I and Osipov S P 1994 *Rus. J. Nondestruct. Testing* **9** 92–95
- [13] Chen F and Wong R J Y 2014 *J. Comput. Appl. Math.* **255** 282–296
- [14] Pease B J *et al* 2012 *Constr. Build. Mater.* **36** 419–429
- [15] Osipov S P *et al* 2015 *Adv. Mat. Res.* **1085** 455–459